Vietnam Journal of Earth Sciences
https://vjs.ac.vn/index.php/jse

Forest cover change mapping based on Deep Neuron Network, GIS, and High-resolution Imagery

Nguyen Thanh Hoan[1], Ho Le Thu[1], Nguyen Van Dung[1], Hoa Thuy Quynh[1], Nguyen Kim Anh[1], Le Duc Hanh[1], Pham Van Duan[4], Trong Trinh Phan[2], Tran Van Phong[2,3*]

[1]Institute of Geography, Vietnam Academy of Science and Technology, Hanoi, Vietnam
[2]Institute of Geological Sciences, Vietnam Academy of Science and Technology, Hanoi, Vietnam
[3]Graduate University of Science and Technology, Vietnam Academy of Science and Technology, Hanoi, Vietnam
[4]Institute for Forest Ecology and Environment, Vietnam National University of Forestry, Hanoi, Vietnam

ABSTRACT

With the rapid advancement of technology, monitoring forest cover changes has become increasingly quantifiable through various techniques and methods. In this study, we developed a procedure that utilizes the Deep Neuron Network (DNN) model and the Geographic Information Systems (GIS) based on high-resolution imagery captured at different time points to create forest cover change maps in Nui Luot, Chuong My, Hanoi. Two RGB (Red-Green-Blue) spectral images were captured by Unmanned Aerial Vehicle (UAV) at two different time points (pre-scene and post-scene) and used to extract information for the DNN model to produce land cover maps for these two time points. The land cover classification was divided into four classes: (1) Trees, (2) Vacant, (3) Built area and others, and (4) Water surface. Combined with GIS analysis, the forest cover change maps were developed to quantify detailed increases or losses in forest cover based on the "Trees" class. The model's accuracy was evaluated using parameters such as the area Under the ROC Curve (AUC), Accuracy (ACC), Precision, Recall, F1-Score, Kappa, and Root Mean Square Error (RMSE). The analysis results indicate that from January 31, 2023, to October 20, 2023, the forest cover in the study area decreased by 0.53%. The accuracy metrics for the pre-change scene were: average AUC = 0.922, ACC = 76.86%, average Precision = 0.743, average Recall = 0.73, average F1-Score = 0.723, Kappa = 0.692, and RMSE = 0.297. For the post-change scene, the accuracy metrics were: average AUC = 0.954, ACC = 81.89%, average Precision = 0.823, average Recall = 0.815, average F1-Score = 0.818, Kappa = 0.758, and RMSE = 0.262. A deforestation scenario was constructed to evaluate the effectiveness of the DNN models in assessing and monitoring forest dynamics.

Keywords: Deep Learning, UAV, forest cover change, Nui Luot, land cover.

1. Introduction

On a global scale, forest cover is continuing to decline due to the impacts of climate change and human activities (Diez et al., 2021; UN, 2024; Weisse, Goldman and Carter, 2024). According to statistics, in 2023 alone, 3.75 million hectares of primary forest were lost (Weisse, Goldman and Carter, 2024). Among the areas most severely affected are the tropical forests of the Amazon

---

*Corresponding author, Email: tphong1617@gmail.com

(Brazil), the Democratic Republic of the Congo (DRC), and Indonesia (Weisse, Goldman and Carter, 2024), with Vietnam also being one of the countries impacted by the gradual loss of forest cover (Cochard et al., 2016). One of the solutions to manage and mitigate deforestation is the application of technologies in forest monitoring (Henry et al., 2015). Remote sensing tools, satellite imagery, Unmanned Aerial Vehicle (UAV) imagery, and artificial intelligence (AI) are being widely utilized for real-time monitoring of forest dynamics, facilitating early detection of illegal logging activities (Buchelt et al., 2024; Dainelli et al., 2021; Ecke et al., 2022; Giang Linh, Dang Kinh and Bui Thanh, 2023; Guimarães et al., 2020; Liu et al., 2021; Pham-Duc, Tran Anh and Tong Si, 2023; Tran Xuan et al., 2023). Forest change maps serve as valuable tools in forest monitoring technology to track and analyze changes in forest area and quality over time (Hansen and Loveland, 2012; Kim et al., 2014). These maps are typically used for (1) Monitoring forest loss and recovery by providing information on deforestation due to logging, agriculture, or other causes, as well as the recovery of areas that have been devastated (Camarretta et al., 2020). (2) Assessing the impacts of climate change to understand better how climate change affects forest ecosystems, including changes in species distribution and forest structure (Yang et al., 2019). (3) Management and conservation to assist forest managers in planning conservation efforts and sustainable management strategies while also identifying areas that require priority protection (Camarretta et al., 2020; Yang et al., 2019). (4) Ecological research by providing data for studies on biodiversity, soil nutrition, and other ecological factors (Hill et al., 2019; Marín et al., 2021).

AI, particularly machine learning and deep learning methods, has opened up new potentials in classifying and predicting changes in forest cover (Diez et al., 2021; Janga et al., 2023; Khan et al., 2017; Khelifi and Mignotte, 2020; Ortega et al., 2019). AI algorithms can learn from historical data and make more accurate predictions about forest cover changes based on various input factors such as remote sensing data, topography, climate, and human activities (Diez et al., 2021; Isaienkov et al., 2021; Janga et al., 2023; Khelifi and Mignotte, 2020; LeCun, Bengio and Hinton, 2015). The application of AI, remote sensing, and GIS in forest cover mapping not only aids in monitoring changes over time but also plays a crucial role in providing early warnings about deforestation (Annus et al., 2021; Watanabe et al., 2021), environmental degradation, and supports policymakers in sustainable forest resource management (Haq et al., 2024; Lechner, Foody and Boyd, 2020). These advanced technologies have contributed to global efforts in forest protection, biodiversity conservation, and mitigating the impacts of climate change (Haq et al., 2024; Janga et al., 2023).

In recent years, research on forest cover changes using imagery from UAV combined with advanced AI tools has become a prominent trend in the fields of remote sensing and environmental monitoring (Diez et al., 2021; Ecke et al., 2022; Mohan et al., 2021). UAV provide high-resolution spatial data and flexibility, allowing detailed information to be collected in hard-to-reach areas (Chenyan et al., 2024; Diez et al., 2021; Ecke et al., 2022; Grubesic, Nelson and Wei, 2024; Guimarães et al., 2020; Mohan et al., 2021). UAV equipped with optical cameras, particularly RGB spectral channels, are widely used due to their cost-effectiveness

and simple data structure (Bourgoin et al., 2020; Diez et al., 2021; Li et al., 2020; Schiefer et al., 2020). Successful applications of deep learning combined with UAV RGB imagery analysis in forest change studies include research by Onishi and Ise (2021), who utilized Convolutional Neural Networks (CNN) to successfully classify seven tree classes with over 90% accuracy at the Kamigamo Experimental Station of Kyoto University (Onishi and Ise, 2021). A similar study employing CNN to analyze high-resolution UAV RGB imagery (Schiefer et al., 2020) accurately mapped nine tree species, three genus-level classes, dead wood, and forest floor with an F1-score accuracy of 0.73 in temperate forest areas of the Southern Black Forest and Hainich National Park in Germany (Schiefer et al., 2020). Xie et al. (2024) used the Mask R-CNN model to create high-accuracy forest maps based on high-resolution UAV RGB images in Jiangle County, Fujian Province, China (Xie et al., 2024). These examples demonstrate the significant potential of applying deep learning models combined with high-resolution UAV RGB imagery analysis for forest cover change identification and mapping.

The DNN serves as a foundational model for deep learning techniques, offering several advantages such as (1) the ability to learn complex features: DNN have multiple hidden layers, allowing them to learn intricate and nonlinear features from data (Aldahdooh et al., 2022; Hussain, Tamizharasan and Rahul, 2022). This makes them suitable for tasks such as image recognition, speech recognition, and natural language processing (Hussain, Tamizharasan, and Rahul, 2022); (2) automatic feature extraction: One of the most significant advantages of DNN is their ability to automatically extract essential features from raw data without human intervention, minimizing reliance on manual feature selection techniques (Du et al., 2018); (3) high performance with large datasets: DNN often outperforms traditional methods when large amounts of data are available for training (Faker and Dogdu, 2019; Rithani, Kumar and Doss, 2023). It can leverage information from large datasets to enhance the accuracy and generalization capabilities of the model (Faker and Dogdu, 2019; Rithani, Kumar and Doss, 2023); and (4) scalability: DNN are flexible and can scale with various data types, from structured data to unstructured data such as images, audio, and text (Aldahdooh et al., 2022; Du et al., 2018; Hussain, Tamizharasan and Rahul, 2022).

With the advantages of DNN models and high-resolution UAV RGB imagery outlined above, this study presents a procedure for applying a DNN model based on high-resolution UAV RGB image analysis and GIS techniques to create forest cover change maps over two different periods. The experimental study area is the Luot Mountain area in Chuong My, Hanoi, with forest cover dynamics analyzed using two optical RGB images captured at different times (pre-scene: January 1, 2023, and post-scene: October 20, 2023). Accordingly, two land cover classification maps were created with four classes (Trees, vacant, built area, and others, as well as water surface). The 'Trees' class was extracted using GIS analysis to develop the forest cover change map for the study area. The results of this research contribute to assisting managers in the planning and rational use of forest land and demonstrate the potential applications for high-accuracy forestry research.

2. Research area

The study area is part of Luot Mountain, covering an area of 209.3 hectares, located in the center of Xuan Mai Town, 38 km from the center of Hanoi, and 45 km from Hoa Binh Town (Fig. 1). Luot Mountain features relatively uniform terrain characterized by low hills, with minimal fragmentation, comprising two contiguous hills extending approximately 2 km from east to west. One peak has an absolute height of 133 m, while the other reaches 76 m, with an average slope of 15 degrees and a maximum slope of 27 degrees. The primary aspects are northeast, northwest, and southeast. The terrain conditions are favorable for afforestation. Several indigenous tree species, such as Diospyros spp, Hopea odorata, and Dalbergia tonkinensis, have been planted in this area. The soil in the Luot Mountain area is yellow-brown Feralit soil developed on the parent rock of Porphyry belonging to the neutral magma rock group, with thickness varying from thick to medium depending on the specific topographical location.

Climate: Luot Mountain is situated within the humid tropical monsoon climate zone, characterized by two distinct seasons: the rainy season from April to October and the dry season from November to March of the following year.

- Temperature Regime: The average annual temperature is 23.2°C, with the highest average monthly temperatures in July and August reaching 28.5°C and the lowest average in January at 16.5°C. The hot season sees temperatures exceeding 25°C from May to mid-September, while the cold season has average temperatures below 20°C from December to March of the following year.

The remaining months have average temperatures ranging from 20 to 25°C.

- Precipitation Regime: The total annual rainfall is 1753 mm, with an average monthly rainfall of 146 mm. Rainfall is unevenly distributed throughout the year, with the highest average monthly rainfall occurring in July and August at 312 mm and the lowest in January at 15 mm.

- Humidity: The average relative humidity is relatively high at 84% but varies significantly between months.

- Evaporation: The average annual evaporation is 602 mm, with the highest in May (78.5 mm) and the lowest in February (47.6 mm).

- Wind Regime: The area is influenced by two main wind directions:

o The Southeast monsoon blows from April to October.

o The Northeast monsoon blew from November to March of the following year.

The area is traversed by two rivers, surrounded by the Bui and Tich rivers, with a total river and stream area of 29.43 hectares. Additionally, there are water reservoirs and dam systems, such as Vai Bon Lake and the Tran Dam.

Flora Resources: The experimental forest at Luot Mountain has recorded 342 species of vascular plants belonging to 257 genera and 90 families. The vegetation in the area is diverse in life forms and values, comprising 9 life forms and 7 value groups.

Fauna Resources: The area has recorded 156 species of vertebrates from 20 orders, 60 families, and 104 genera, including 21 rare species. Furthermore, 409 insect species have been identified from 87 families and 13 orders, with the order Lepidoptera accounting for 208 species, 135 genera, 30 families, 10 classes, and 4 species.
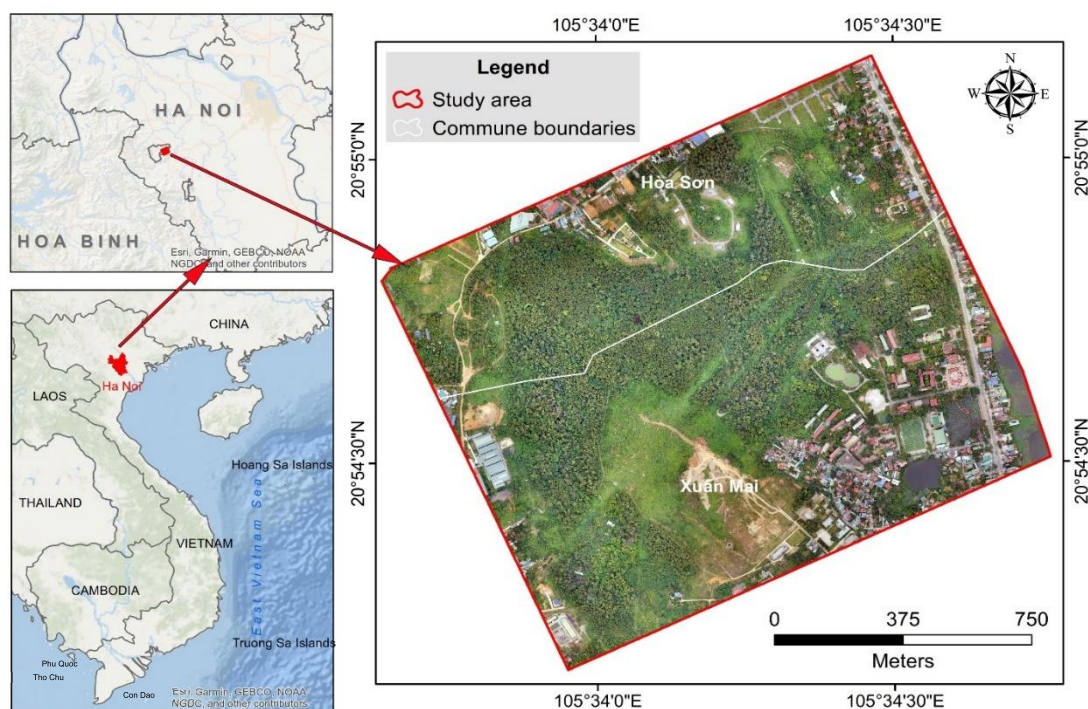
Figure 1. Study area in a part of Luot mountain, Chuong My, Hanoi

3. Methodology and data used

3.1. Methodology

The research methods and techniques employed are illustrated in an 8-step process (Fig. 2). The sequence of steps is as follows:

Step 1: Select the study area at Luot Mountain (Fig. 1).

Step 2: Collect the database: Gather UAV imagery with RGB spectral channels at two different time points (Fig. 2). Details about the collected data are presented in the data section.

Step 3: Sample data for the model: Samples are determined based on location through analysis of the imagery and verified through fieldwork. Thus, the input data for the model includes 3 RGB bands. The label data comprises 4 classes: (1) Trees, (2) Vacant, (3) Built area and others, and (4) Water surface. These sample data are organized into two approaches: Option 1 separates training and validation datasets for each imagery

scene. Option 2 combines the training data of the pre-scene and post-scene into a single training dataset while maintaining the validation datasets for each imagery scene.

Step 4: Model implementation using a DNN model applied through the WekaDeeplearning4j tool in Weka software version 3.8.6 (Lang et al., 2019). This tool features an intuitive and user-friendly graphical user interface (GUI) that is easy to use.

Step 5: Evaluate the model results using assessment parameters for multi-class classification problems, such as ROC, AUC-ROC, Accuracy, Precision, F1-Score, Recall, Kappa, and RMSE.

Step 6: Select the optimal option based on the model evaluation results from Step 5. In this study, Option 1 was chosen to facilitate the creation of the land cover map. An additional scenario to verify the model's accuracy assumes areas of lost forest cover in the post-scene imagery (Fig. 3). Accordingly, these areas in the post-scene are color-coded

in gray, and a land cover map based on this scenario is established.

Step 7: Create the land cover map based on the DNN model from the pre- and post-scene. A land cover map verifies the model after

classification is created according to the deforestation scenario.

Step 8: Use GIS technology to analyze and develop a forest cover change map. The tool utilized is ArcMap 10.8 [ESRI Inc].
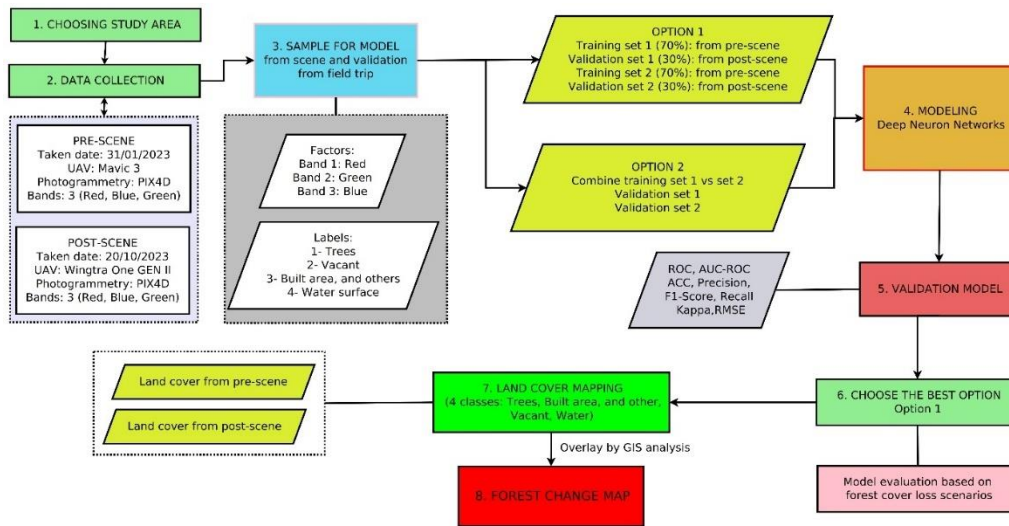

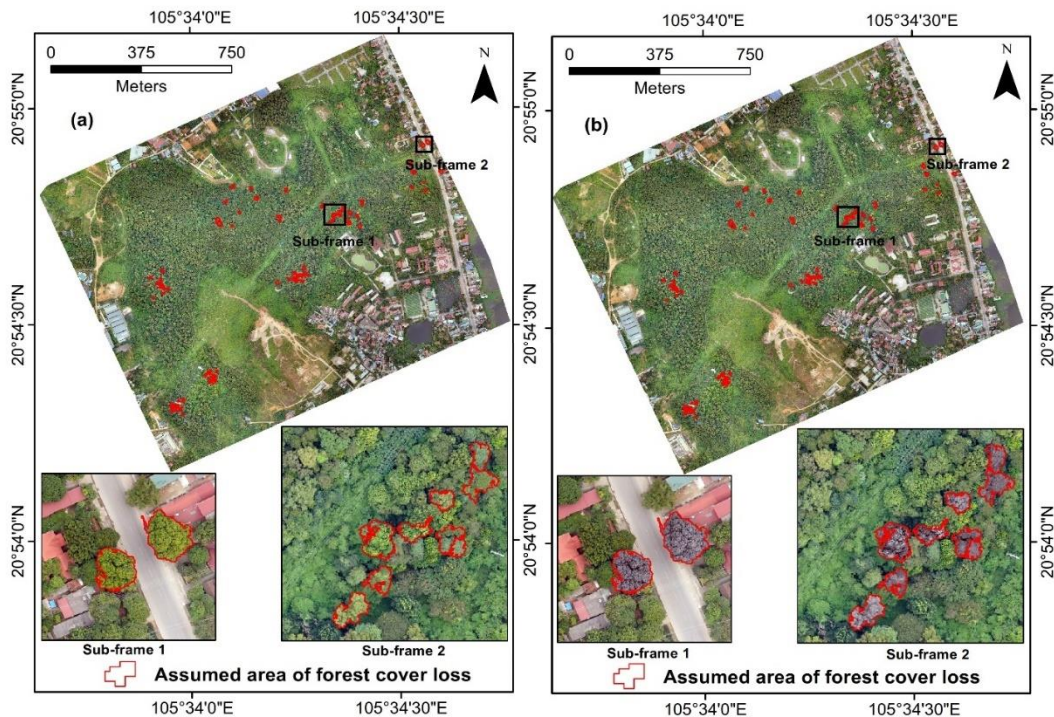*Figure 2.* Flow chart processing in this study

Figure 3. Delineation of areas for the hypothetical deforestation scenario: (a) post-scene, (b) the scene after revision according to the deforestation script of the post-scene

3.1.1. Generating photogrammetry imagery from UAV images

The basic steps to create maps from UAV imagery include:

(1) Data Collection: Fly the UAV over the area of interest and collect aerial images with an inevitable overlap between them.

(2) Data Preprocessing: Perform basic edits on the images, such as color balancing, noise reduction, and brightness adjustment.

(3) Image Stitching: Use PIX4D software to stitch the images into a sizeable ortho mosaic image (Caputo et al., 2023). The software employs algorithms to identify common points between the images and merge them (Caputo et al., 2023).

(4) Georeferencing: Assign spatial coordinates to the stitched image to create a map that can be utilized in GIS.

3.1.2. Deep Neuron Network model

DNN is characterized by a structure that includes multiple layers, particularly hidden ones (Liu et al., 2017; Shrestha and Mahmood, 2019). These networks are widely used in AI and machine learning to model complex relationships in data (Liu et al., 2017). The operation of DNN relies on neurons and their connections (LeCun, Bengio, and Hinton, 2015). Each neuron in a layer receives input from the neurons of the previous layer, computes the output, and transmits the result to the next layer (Shrestha and Mahmood, 2019). The network learns to adjust weights through a training process using the backpropagation algorithm and optimizes them using algorithms like gradient descent (Shrestha and Mahmood, 2019). DNN is notable for its ability to automatically learn features from complex and nonlinear data, which traditional models struggle to handle (Samek et al., 2017). DNN form the foundation of deep learning algorithms, enabling them to tackle various tasks ranging from computer vision to natural language processing (Liu et al., 2017). Figure 4 illustrates how the DNN model classifies land cover from UAV RGB images. Table 1 presents the hyperparameters of the DNN model used in this study.
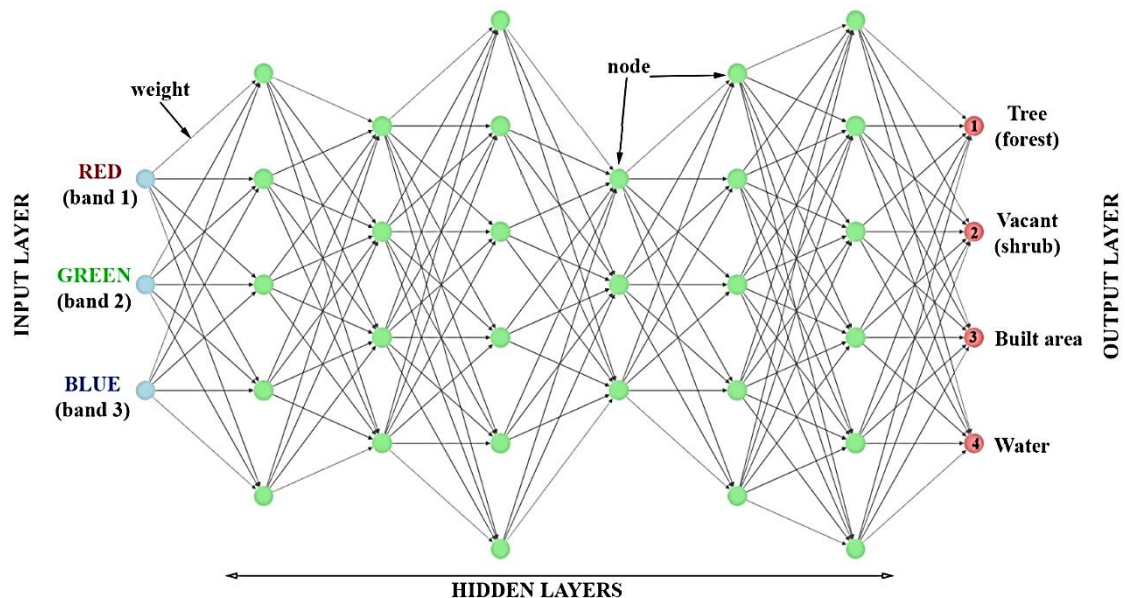

Figure 4. Illustration of the multilayer neural network of Deep Learning for classifying forest cover from high-resolution UAV imagery in the Luot Mountain area

Table 1. The hyperparameters of the DNN model

Hyperparameters	Feature/Value
Layer specification	
Input layer	3 node
Number of hidden layers	6
Number of nodes in hidden layers	29
Output layer	4 node
Connection	full
Activation	Softmax
Loss function	MCXENT
Number of epochs	10
Batch size	100
Network configuration	
Optimization algorithm	Stochastic gradient descent
Updater	Adam
Bias Updater	Sgd
Learning rate	0.001
Weight initialization method	XAVIER
Bias initialization	0.0

Basic Structure of DNN

Input Layer: Receives input data and passes it to the hidden layers. Each neuron in the input layer corresponds to a feature of the data.

- Hidden Layers: These layers lie between the input and output layers, where complex computations occur. Each hidden layer consists of multiple neurons, allowing the network to learn more abstract and complex features.

- Output Layer: Provides the network's final results. Depending on the type of problem, the output layer may represent probabilities for classification classes or continuous values for regression tasks.

Activation Functions

Activation functions are crucial components in DNN that help the network learn the nonlinear characteristics of the data:

- ReLU (Rectified Linear Unit): Commonly used in hidden layers, the formula ReLU facilitates faster learning and mitigates the vanishing gradient problem.

- Sigmoid: Maps input values to a range between 0 and 1, typically used for binary classification.

- Tanh: Converts input values to a range between -1 and 1, enabling faster and more stable learning than Sigmoid.

- Softmax: Converts outputs into probabilities for multi-class classification.

Training Process

- Forward Propagation: The process of passing data through the network's layers to compute the output.

- Loss Function: Measures the difference between the network's predictions and the actual values. For example, MSE (Mean Squared Error) is used for regression, and Cross-Entropy is used for classification.

- Backpropagation: Computes the gradient of the loss function to the network's weights and updates the weights using optimization algorithms.

Optimization Algorithms

- Gradient Descent: Adjusts weights in the direction of the negative gradient of the loss function to minimize loss.

- Adam (Adaptive Moment Estimation): A more efficient optimization algorithm that adjusts the learning rate based on the first and second moments of the gradient.

Regularization

Techniques to prevent overfitting and improve the network's generalization ability:

- Dropout: Randomly removes some neurons during training to prevent the network from relying too heavily on certain neurons.

- L2 Regularization: Adds a penalty to the loss function based on the sum of the squares of the weights, helping to reduce model complexity.

3.1.3. Methods for evaluating model accuracy

To evaluate the accuracy of the DNN model in the land cover classification task, the evaluation metrics used in this study include the Confusion Matrix, Area Under the Curve (AUC), Accuracy, Precision, Recall, F1-Score, Kappa, and RMSE (Maxwell et al., 2017; Rodriguez-Galiano and Chica-Rivas, 2014).

Confusion Matrix

The Confusion Matrix is a machine learning tool used to assess a classification

model's performance. This matrix displays the number of predictions made by the model for each class, allowing for a comparison between the predictions and the actual values (Marom, Rokach, and Shmilovici, 2010). The structure of a 4-class confusion matrix C for the land cover classification problem in this study is as follows:

$$C = \begin{bmatrix} C_{11} & C_{12} & C_{13} & C_{14} \\ C_{21} & C_{22} & C_{23} & C_{24} \\ C_{31} & C_{32} & C_{33} & C_{34} \\ C_{41} & C_{42} & C_{43} & C_{44} \end{bmatrix} \quad (1)$$

where: C_{ii} (với i = 1, 2, 3, 4) is the number of correct predictions for each corresponding class (Vacant; Water; Built area and others; Trees). C_{ij} ($i \neq j$) is the number of incorrect predictions, meaning samples belonging to class i but incorrectly predicted as class j.

Accuracy (ACC)

The accuracy parameter is a commonly used measure to evaluate the performance of classification models in machine learning and artificial intelligence. It measures the ratio of correct predictions to the total number of predictions. Accuracy indicates the percentage of data samples the model can correctly classify (Rodriguez-Galiano and Chica-Rivas, 2014). The formula for calculating accuracy is as follows:

$$\text{Accuracy} = \frac{\sum_{i=1}^{4} C_{ii}}{\sum_{i=1}^{4} \sum_{j=1}^{4} C_{ij}} \quad (2)$$

where: $\sum_{i=1}^{4} C_{ii}$ is the total number of correct predictions for all classes (which is the sum of the elements on the main diagonal of the confusion matrix). $\sum_{i=1}^{4} \sum_{j=1}^{4} C_{ij}$ is the total number of data samples (which is the sum of all elements in the confusion matrix).

Precision

Precision measures the ratio of true positive predictions to all positive predictions. It is primarily used when we are interested in positive results and want to minimize false positive predictions (Maxwell et al., 2017). The precision for class i is calculated using the formula:

$$\text{Precision}_i = \frac{C_{ii}}{C_{ii} + \sum_{j \neq i} C_{ji}} \quad (3)$$

where: The numerator C_{ii} represents the total number of predictions for class i (both correct and incorrect). The denominator is the sum of C_{ii} and all values C_{ji}, which accounts for false positive predictions from other classes incorrectly predicted as class i.

Recall

Recall measures the ratio of actual positive samples that are correctly predicted. It is crucial when we want to minimize cases of missed detections (False Negatives) (Maxwell et al., 2017). The recall for class iii is calculated using the formula:

$$\text{Recall}_i = \frac{C_{ii}}{C_{ii} + \sum_{j \neq i} C_{ij}} \quad (4)$$

where: The numerator C_{ii} represents the number of correct predictions for class i. The denominator is the sum of C_{ii} and all values C_{ij}, which accounts for false negative predictions from other classes incorrectly predicted as another class.

F1-Score

F1-score is the harmonic mean between precision and recall, helping to balance the two measures. The F1-score is particularly useful in cases of imbalanced data (Draszawka and Szymański, 2023). The formula for calculating the F1-score for class i is:

$$F1 - score_i = 2 \times \frac{Precision_i \times Recall_i}{Precision_i + Recall_i} \quad (5)$$

Area Under Curve (AUC)

AUC is a common metric for evaluating the performance of classification models, typically used for binary classification tasks. For multi-class classification problems, AUC is extended by calculating the AUC for each class and then aggregating these values (Wu and Zhou, 2017). In this context, the multi-class classification problem is transformed into several binary classification problems. Specifically, for each class, you compare that class against all other classes combined into a single class (Wu and Zhou, 2017). The AUC for each class is then calculated similarly to the binary case. The closer the AUC value is to 1, the more accurate the model.

Steps to calculate AUC for each class:

- Select a class *i*, then label this class as positive (Positive) and the remaining classes as negative (Negative).

- Calculate the true positive rate (TPR) and false positive rate (FPR) for each class *i*.

The formula for calculating AUC for each class is as follows:

$$AUC_i = \sum_{k=1}^{n-1} \frac{(TPR_{k+1} + TPR_k)}{2}(FPR_{k+1} - FPR_k) \quad (6)$$

where: TPR is the true positive rate (recall); FPR is the false positive rate. nnn is the total number of samples in class *i*.

The mean AUC value across classes is calculated by summing the AUCs for each class and dividing by the number of classes.

Kappa

Kappa measures the accuracy of the model while accounting for random factors. It assesses the agreement between the model's predictions and the actual labels, adjusting for any random outcomes that may occur (de la Torre, Puig and Valls, 2018). The formula for Kappa is:

$$Kappa = \frac{p_0 - p_e}{1 - p_e} \quad (7)$$

where p_0 is the proportion of correct predictions made by the model, and p_e is the expected proportion of correct predictions due to chance, calculated by taking the product of the total number of correct predictions and the total number of actual predictions for each class.

Root Mean Square Error (RMSE)

RMSE measures the deviation between predicted and actual values, which is commonly used in regression problems. It represents the model's error level, with a smaller RMSE indicating better model performance (Wei and James, 2013). The formula for RMSE is:

$$RMSE = \sqrt{\frac{1}{n}\sum_{i=1}^{n}(y_i - \widehat{y_i})^2} \quad (8)$$

where y_i is the actual value of the *i*-th sample, $\widehat{y_i}$ is the predicted value of the *i*-th sample, and *n* is the total number of data samples.

3.2. Data used

3.2.1. High-solution UAV images

The primary database in this study consists of two photogrammetry image scenes (Fig. 5), captured at two different time points (pre-scene: captured on January 31, 2023 (Fig. 5a) and post-scene: captured on October 20, 2023 (Fig. 5b)). The data for pre-scene was processed using images taken from a Mavic 3 drone (Fig. 6a) (Chenyan et al., 2024). Post-scene was processed using images from a Wingtra One GEN II drone (Fig. 6b) (Grubesic, Nelson, and Wei, 2024). The specifications of the two drones are presented in Table 2. Both scenes were processed to achieve an ordinary spatial resolution of 0.1266 m/pixel, with each image comprising three RGB spectral bands.
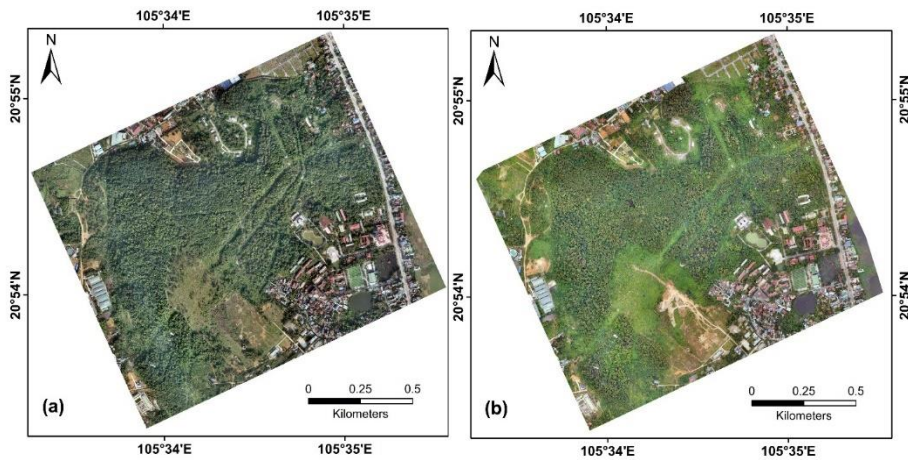

Figure 5. The photogrammetry scenes in the study area: (a) pre-scene, (b) post-scene

Figure 6. Images of the drones used in this study: (a) Mavic 3 (source: https://www.dji.com) and (b) WingtraOne GEN II (source: https://wingtra.com/)

Table 2. Basic technical specifications of the Mavic 3 and WingtraOne GEN II drone

	Mavic 3	**WingtraOne GEN II**
Flight Specifications		
Takeoff Weight	895 g (takeoff state)	4.5 kg (takeoff state)
Maximum Flight Distance	15000 m	10000 m
Maximum Flight Speed	21 m/s	16 m/s
Maximum Flight Time	46 minutes	59 minutes
Frequency	2.4–5.8 GHz	2.4–5.8 GHz
Operating Temperature	-10°C–40°C	-10°C–40°C
Maximum Altitude	6000 m	5000 m
Camera		
Sensor	CMOS 4/3, effective pixels: 20 MP	APS-C sensor (23.5 × 15.6 mm), effective pixels: 24.2 MP.
Image Size	5280 × 3956	6000 × 4000
Image Format	JPEG / DNG (RAW)	JPEG, RAW
GNSS		
Satellite System	GPS + Galileo + BeiDou	GPS (L1, L2), GLONASS (L1, L2), Galileo (L1) and BeiDou (L1)

Source: https://www.dji.com and https://wingtra.com/.

3.2.1. Samples for model

Sampling was conducted by delineating polygonal areas on images (both pre-scene and post-scene), with validation from field verification (Fig. 7). For each scene, samples were collected according to each class (Trees; Vacant; Built area, others; and Water surface), with 100 polygons taken per class. In total, 400 polygons were sampled for each scene. These polygons were labeled according to their classes and divided into sample points using GIS analysis. Two sampling strategies were implemented to generate data for the DNN model: Option 1 consisted of four datasets: (1) the training dataset for the

pre-scene, comprising 70% of the data (7846 points), (2) the validation dataset for the pre-scene, comprising 30% of the data (3362 points), (3) the training dataset for the post-scene, comprising 70% of the data (7872 points), and (4) the validation dataset for the post-scene, comprising 30% of the data (3373 points). Option 2 merged the two training datasets from Option 1 into a single training dataset (15718 points), while the validation datasets remained unchanged as per Option 1. Consequently, the validation results of the model based on the more optimal option will be utilized for modeling land cover mapping in the study area.
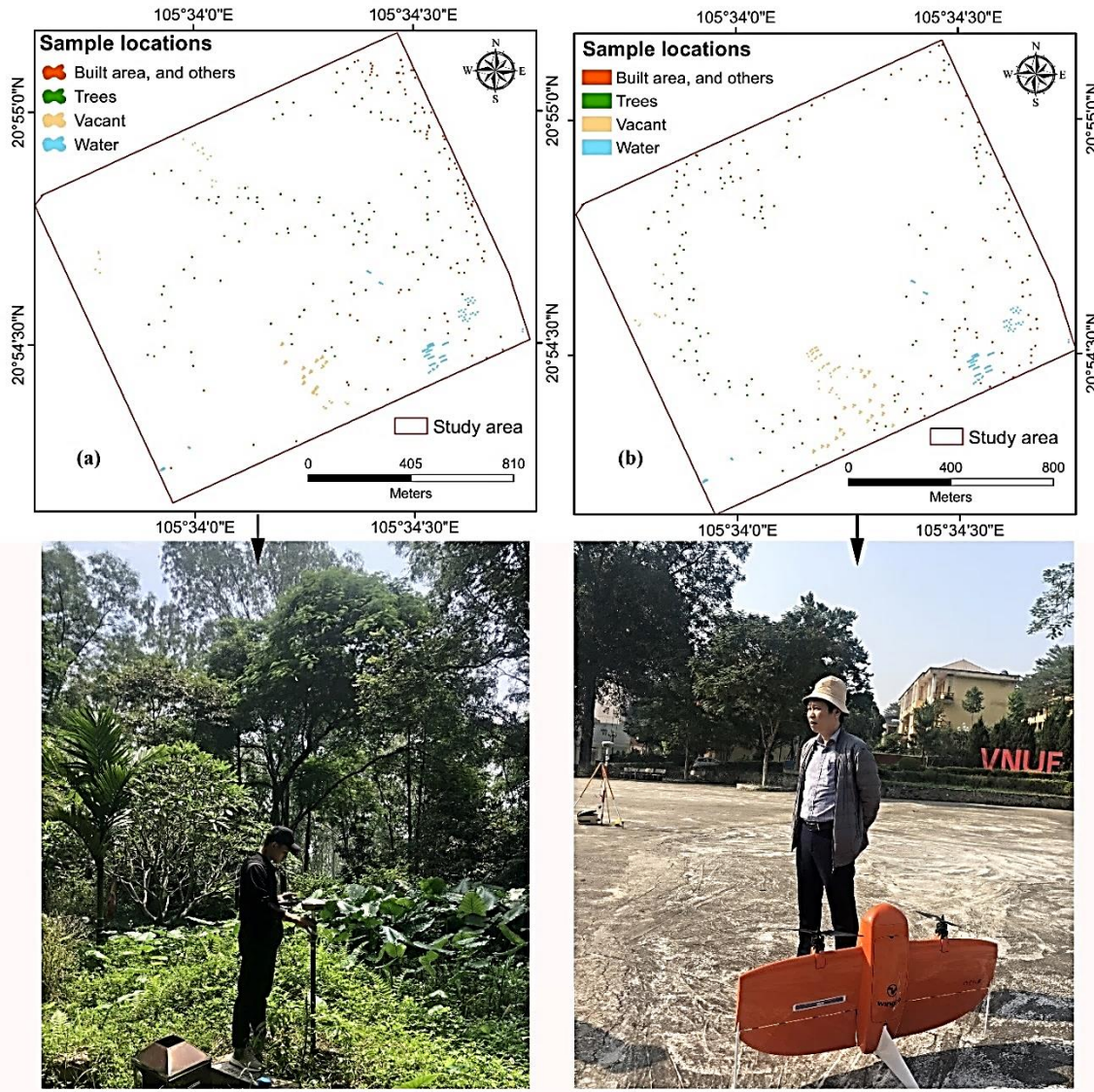
Figure 7. Sampling location maps and some photos of field sampling activities in the study area:
(a) pre-scene, (b) post-scene (Photographer: Nguyen Van Dung)

4. Results

4.1. Selection of model training approaches and evaluation results

Two options are presented in sections 3.1 and 3.2.1 to select the most optimal option for establishing the land cover map in the study area. The results are primarily evaluated based on comparisons using a validation dataset through multi-parameter analysis. The evaluation parameters include AUC, ACC, Precision, Recall, F1-Score, Kappa, and RMSE. Figure 8 details the AUC results calculated based on the ROC curve for the training and validation datasets of the two Options. The AUC mean value for the training dataset of the pre-scene is AUC = 0.925 (Fig. 8a), for the post-scene is AUC = 0.955 (Fig. 8c), and for the combined training dataset, it is AUC = 0.933 (Fig. 8e). The AUC

training results indicate that the training models for both Options demonstrate high accuracy. The AUC for the combined training dataset (Fig. 8e) falls between the training datasets 1 and 2 (Figs. 8a, c). The AUC values for the validation datasets also reflect the high accuracy of the DNN model, with the average AUC for the validation dataset of Option1 for the pre-scene is 0.922 (Fig. 8b) and for the post-scene (AUC mean = 0.954) (Fig. 8d); for Option 2, the pre-scene has a mean AUC of 0.920 (Fig. 8f) and the post-scene has a mean AUC of 0.952 (Fig. 8g). The validation results indicate that the AUC values for the pre-scene and post-scene in Option 2 (Figs. 8f, g) are lower than those in Option 1 (Figs. 8b, d).

According to the accuracy evaluation results, the ACC for the training dataset of the pre-scene is 76.63%, for the post-scene is 81.85%, and for the combined training dataset is 77.17% (Table 3). The ACC value for the combined training dataset in Option 2 lies between the ACC values of the pre-scene and post-scene in Option 1 (Table 3). Examining the ACC values on the validation dataset for both options shows that the validation results for the pre-scene (ACC = 72.58%) and post-scene (ACC = 81.50%) in Option 2 are lower than those in Option 1, which have ACC values of 76.86% and 81.89%, respectively (Table 3). For the Kappa values, the training datasets in Option 1 yield Kappa values of 0.688 for the pre-scene and 0.758 for the post-scene (Table 3). In contrast, the combined training dataset in Option 2 has a Kappa value of 0.696 (Table 3). The Kappa values for the validation datasets in Option 1 are 0.692 for the pre-scene and 0.758 for the post-scene, while in Option 2, the Kappa values for the pre-scene and post-scene are 0.635 and 0.753, respectively (Table 3). Similar to the ACC results, the Kappa evaluations also indicate that Option 1 outperforms Option 2, with higher validation values for both scenes (Table 3). The RMSE values for the validation

datasets in Option 1 are lower for the pre-scene (RMSE = 0.297) and post-scene (RMSE = 0.261) compared to Option 2, which has RMSE values of 0.310 for the pre-scene and 0.268 for the post-scene (Table 3). Overall, the evaluations from the three metrics ACC, Kappa, and RMSE indicate that both the training and validation models demonstrate high reliability for the DNN model, with the results from option 1 being superior to those from option 2.

The evaluation results using precision, recall, and F1-score for each class based on the training data of both options are detailed in Fig. 9. The precision values for the training dataset of the pre-scene are as follows: Trees (0.68), Vacant (0.88), Built area, and others (0.89), and Water surface (0.65) (Fig. 9a). For the post-scene, the precision values are Trees (0.83), Vacant (0.80), Built area, and others (0.83), and Water surface (0.81) (Fig. 9b). The combined training dataset shows precision values of: Trees (0.72), Vacant (0.85), Built area, and others (0.87), and Water surface (0.68) (Fig. 9c). These precision values across all classes indicate that the DNN model is highly accurate. The average precision for the four classes is 0.775 for the pre-scene, 0.818 for the post-scene, and 0.78 for the combined dataset. Similarly, the recall results presented in Fig. 9 indicate that the average recall for the four classes in the pre-scene training dataset is 0.768, in the post-scene, 0.82, and for the combined training dataset is 0.773. The average F1-score for all four classes (Trees; Vacant; Built area, and others; Water surface) is 0.77 for the pre-scene, 0.815 for the post-scene, and 0.778 for the combined dataset. Overall, according to the evaluation parameters of precision, recall, and F1-score, the training values for Option 2 are positioned between the pre-scene and post-scenes from Option 1. The results indicate that the DNN model exhibits strong and reliable performance across the training datasets.
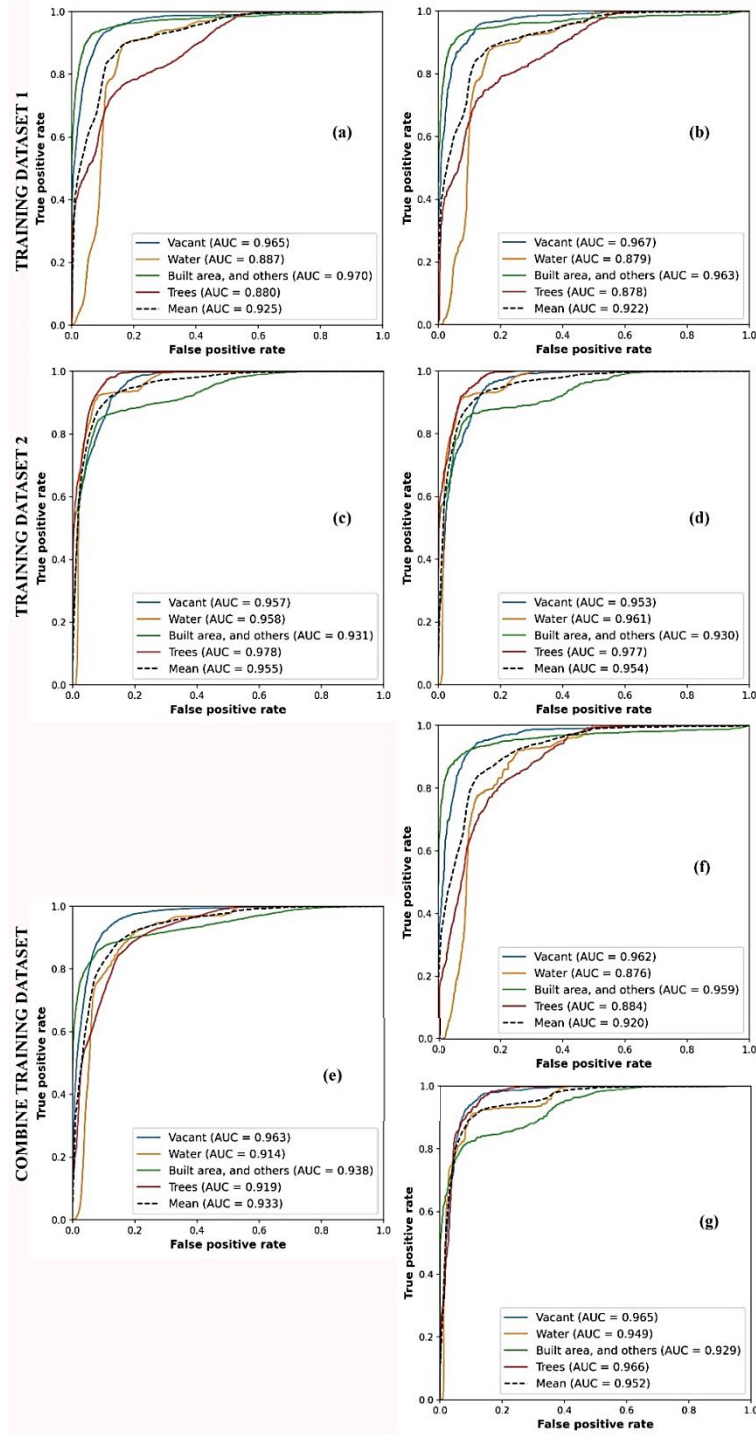
Figure 8. Evaluation results of the DNN model's performance based on the AUC: (a), (b) training and validation datasets for the pre-scene, (c), (d) training and validation datasets for the post-scene, (e) combined training dataset of both scenes, (f), (g) validation datasets for the pre-scene and post-scene based on the combined training dataset

Table 3. Evaluation results of the DNN model based on the metrics ACC, Kappa, and RMSE

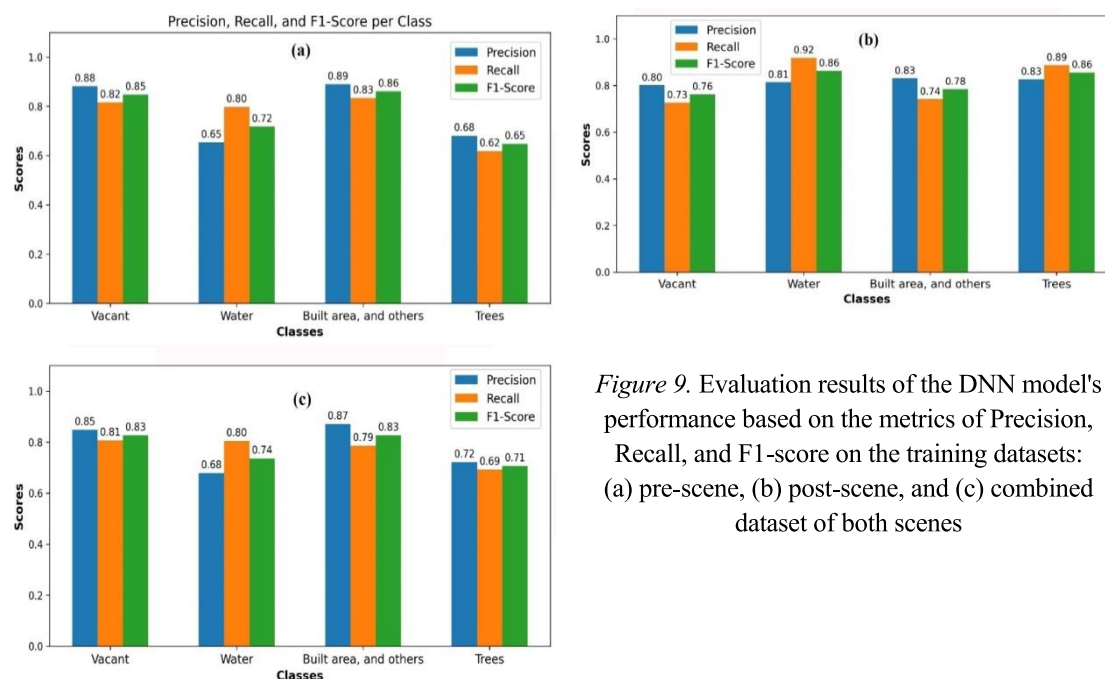| Parameters	Training set 1		Training set 2		Combine training set		
	Training	Validation	Training	Validation	Training	Validation 1	Validation 2
Accuracy	76.63	76.86	81.85	81.89	77.17	72.58	81.50
Kappa	0.688	0.692	0.758	0.758	0.696	0.635	0.753
RMSE	0.294	0.297	0.261	0.262	0.288	0.310	0.268

Figure 9. Evaluation results of the DNN model's performance based on the metrics of Precision, Recall, and F1-score on the training datasets: (a) pre-scene, (b) post-scene, and (c) combined dataset of both scenes

Figure 10 presents the evaluation results of the model based on the validation datasets for Options 1 and 2 according to the metrics of precision, recall, and F1-score. For the validation dataset of the pre-scene in Option 1 (Fig. 10a), the precision values for the classes (Trees; Vacant; Built area, and others; Water surface) are 0.69, 0.88, 0.90, and 0.63, respectively. The recall values are 0.61, 0.84, 0.83, and 0.79, and the F1-scores are 0.65, 0.86, 0.87, and 0.71 (Fig. 10a). The average precision, recall, and F1-score values are 0.78, 0.77, and 0.77, respectively. In the validation dataset for the pre-scene in Option 2 (Fig. 10c), the precision values for the classes are 0.69, 0.85, 0.88, and 0.55, respectively. The recall values are 0.42, 0.83, 0.86, and 0.81, and the F1-scores are 0.52, 0.84, 0.87, and 0.66 (Fig. 10c). The average precision, recall, and F1-score are 0.74, 0.73, and 0.72, respectively. These results indicate that the evaluation values for the pre-scene dataset in Option 1 are better than those in Option 2. For the validation dataset of the post-scene in Option 1 (Fig. 10b), the precision values for the classes are 0.82, 0.80, 0.83, and 0.83, respectively. The recall values are 0.89, 0.73, 0.74, and 0.92, and the F1-scores are 0.85, 0.76, 0.79, and 0.87 (Fig. 10b). The average precision, recall, and F1-score values are 0.820, 0.820, and 0.818, respectively. In the validation dataset for the post-scene in Option 2 (Fig. 10d), the precision values for the classes are 0.73, 0.83, 0.89, and 0.84,

171

respectively. The recall values are 0.93, 0.82, 0.72, and 0.79, and the F1-scores are 0.82, 0.83, 0.80, and 0.82 (Fig. 10d). The average precision, recall, and F1-score are 0.822, 0.815, and 0.817, respectively. The average results indicate that the evaluation values for the post-scene dataset in Option 1 are similar to those in Option 2.

In summary, the evaluation results based on the parameters above indicate that Option 1 is optimal and outperforms Option 2. Consequently, Option 1 has been selected for training and validating the DNN model for each specific view (pre-scene and post-scene) to create land cover maps for each scene.
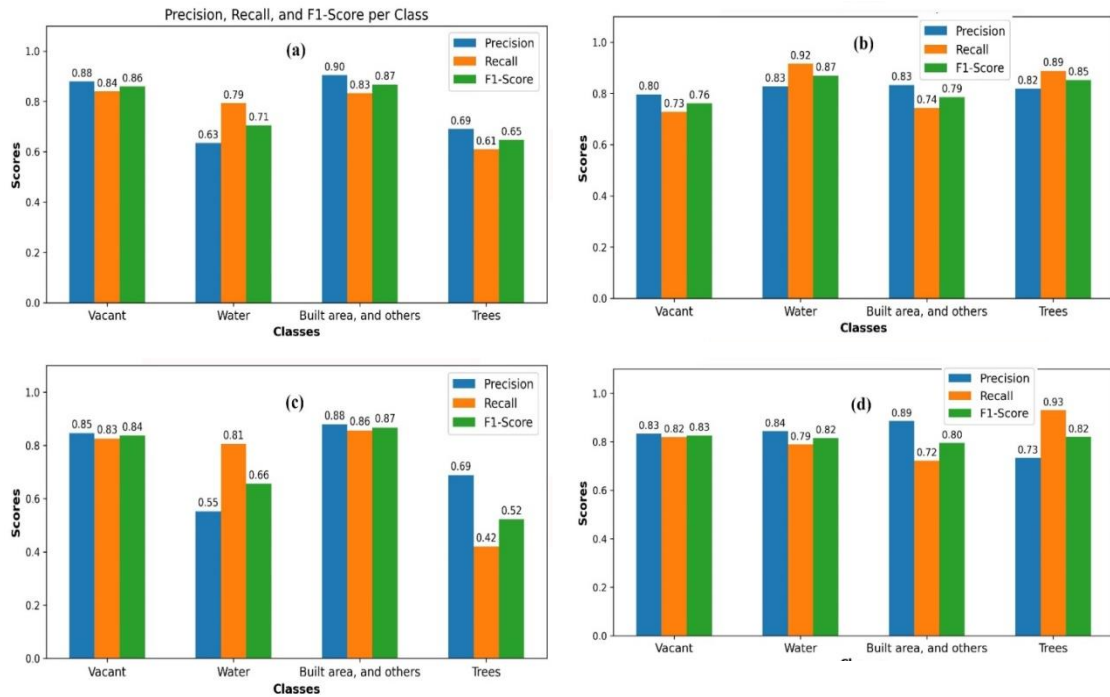

Figure 10. Evaluation results of the DNN model's performance based on the metrics of Precision, Recall, and F1-score on the validation datasets: (a) pre-scene, (b) post-scene, (c) validation dataset for the pre-scene, and (d) validation dataset for the post-scene based on the combined training dataset

4.2. Land cover and forest cover change mapping

As presented in section 4.1, Option 1 was selected to create land cover maps for each scene in the study area. Figure 11 shows the land cover map results using the DNN model based on high-resolution UAV RGB imagery for the pre-scene (Fig. 11a) and post-scene (Fig. 11b). Each land cover map is categorized into four spatial distribution classes: Trees; Vacant; Built area, and others; and Water surface. By comparing the area information of these classes, it is possible to identify changes in land cover. The results of land cover changes are detailed in Table 4. During the period between the two imagery dates (from January 31, 2023, to October 20, 2023), the 'Trees' class decreased by 0.33% in

172

area, the 'Vacant' class increased by 1.44%, the 'Built area and Others' class decreased by 1.68%, and the 'Water surface' class increased by 0.56% (Table 4). To assess forest cover change, the 'Trees' class, which represents forest cover, was separately extracted into forest cover maps for the pre-scene (Fig. 12a) and post-scene (Fig. 12b). Each forest cover map is formatted as a raster, with 'Trees' pixels assigned a value of '1' and 'Non-trees' pixels assigned a value of '0' (Figs. 12a, b). The forest cover change map results were determined by performing a raster subtraction

of the pre-scene forest cover map from the post-scene forest cover map (Fig. 12c). Pixels with a value of '-1' indicate that forest cover has increased compared to the previous period, pixels with a value of '0' indicate no change in forest cover and pixels with a value of '1' indicate that forest cover has been lost (Fig. 12c). To further evaluate the accuracy after classification of the DNN model, a deforestation scenario change map was created to compare the results of the forest change map with actual conditions (Figs. 13, 14).
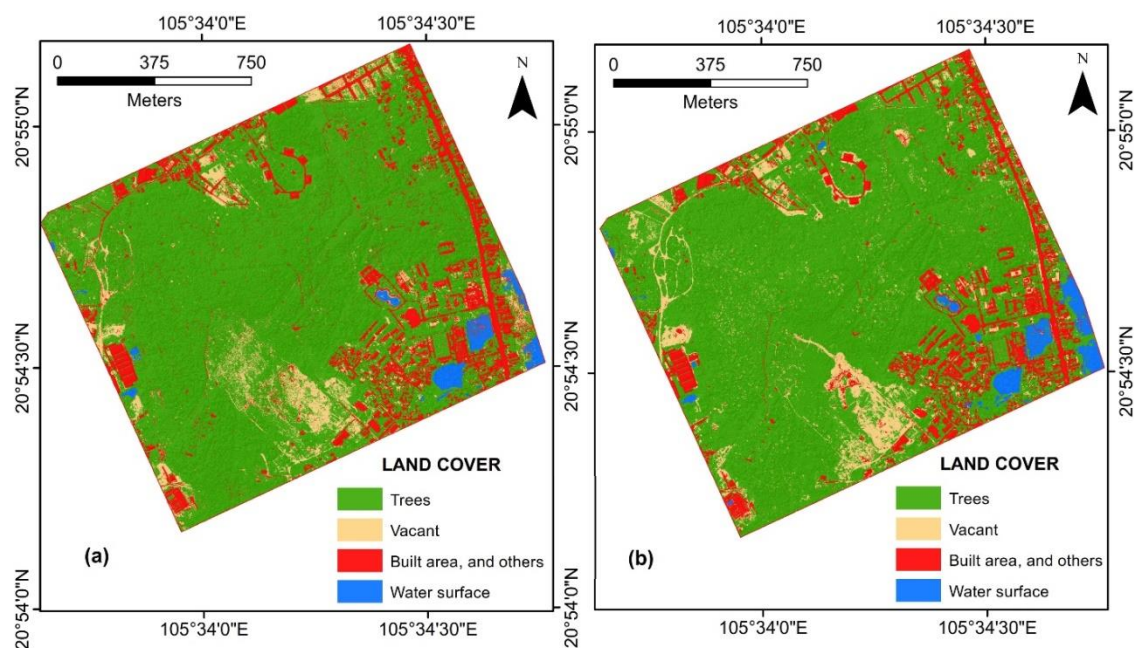

Figure 11. Land cover map results using the DNN model based on high-resolution UAV imagery in the Nui Luot area at two different time points: (a) pre-scene, and (b) post-scene

Table 4. The land cover changed between before and after time

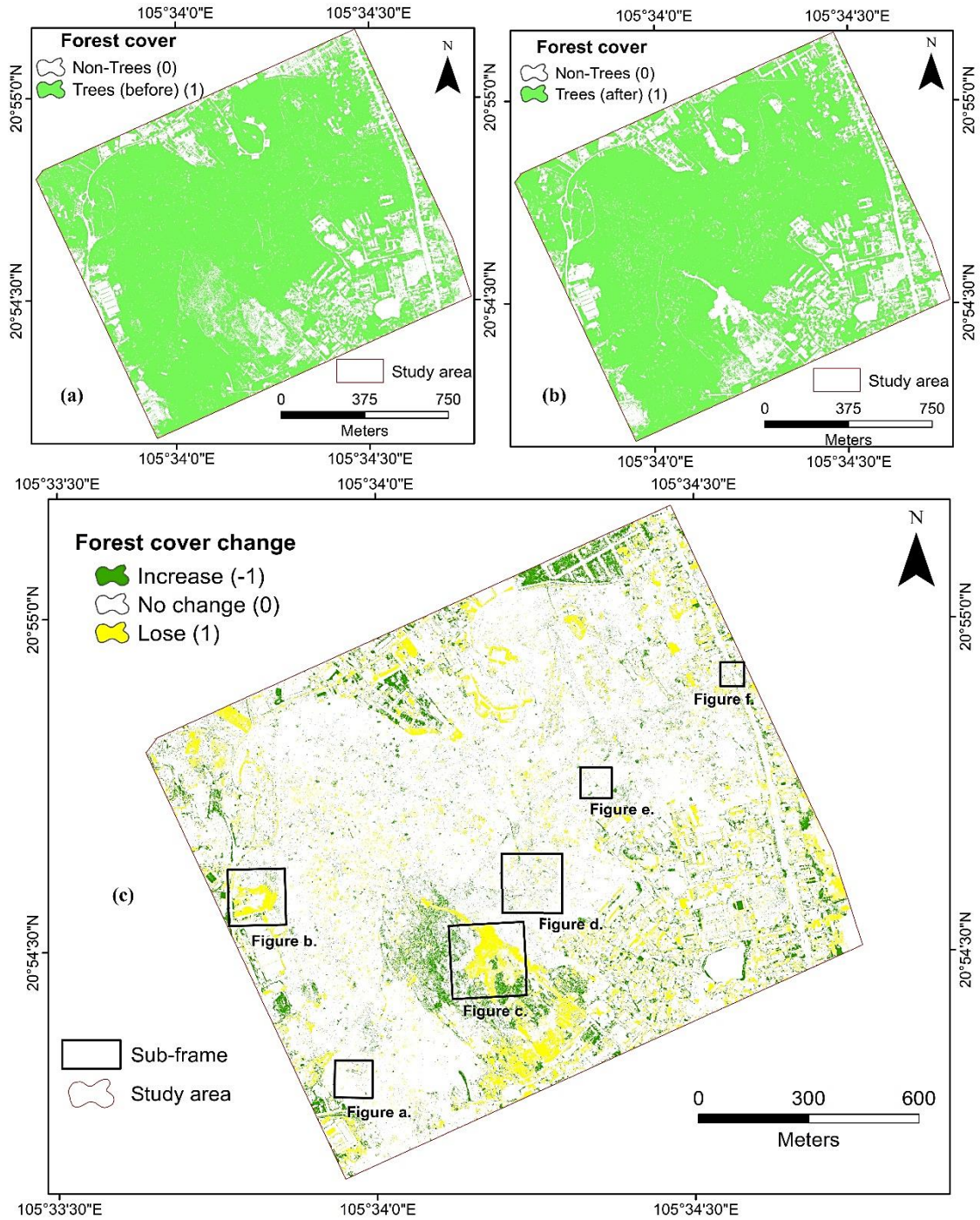| Landcover	Before (B)		After (A)		Variation (A-B)	
	Area (m²)	Percentage (%)	Area (m²)	Percentage (%)	Area (m²)	Percentage (%)
Trees	1.613.879,3	77,11	1.607.114,8	76,78	-6.764,5	-0,33
Vacant	151.994,5	7,26	182.193,5	8,70	30.199,0	1,44
Built area, and other	291.916,3	13,95	256.852,3	12,27	-35.064,0	-1,68
Water	35.147,5	1,68	46.927,0	2,24	11.779,5	0,56

Figure 12. Forest cover change map based on GIS analysis in the study area for the two imagery dates: (a) Forest cover map for the pre-scene, (b) Forest cover map for the post-scene, (c) Forest cover change map between January 31, 2023, and October 20, 2023
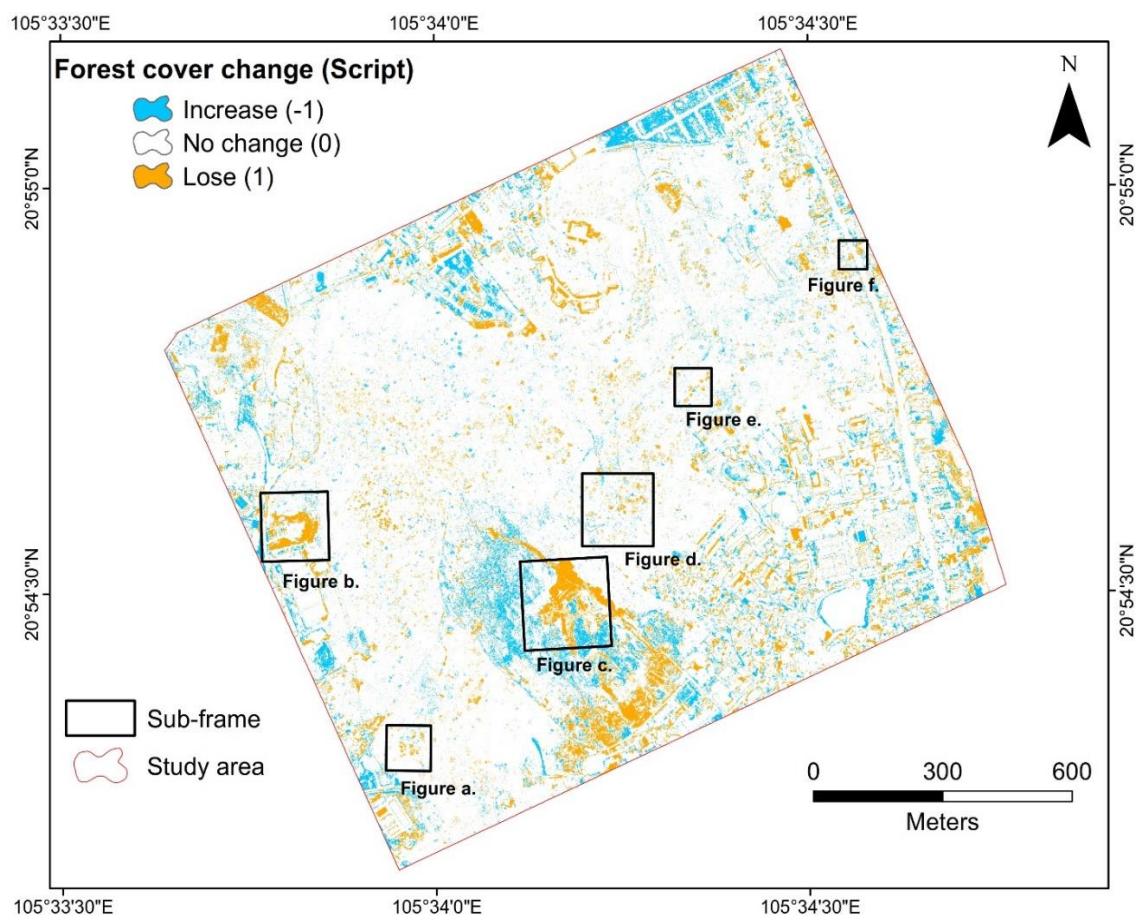
Figure 13. Forest cover change map according to the deforestation scenario in the post-scene compared to the pre-scene

5. Discussions

According to the two selected Options for building the datasets, the combined training dataset of Option 1, despite having a larger sample size (15,718 points) compared to the training datasets of Option 2 (pre-scene: 7,846 points and post-scene: 7,872 points), yielded lower evaluation results on both validation datasets (Section 4.1). Two main factors can explain this: first, there is a difference in color due to the two images being captured at different times during different seasons (the pre-scene was taken on January 31, 2023, in

spring, while the post-scene was taken on October 20, 2023, in autumn). Consequently, the color of the vegetation cover also changes with the seasonal variations in leaf colors. Second, the pre-scene was captured using the Mavic 3 UAV sensor, while the post-scene was captured with the Wingtra One GEN II UAV sensor. These are two types of UAVs with varying technical specifications (Table 2). These two reasons explain why the training dataset does not exhibit as distinctive properties as the training datasets dedicated to each scene.
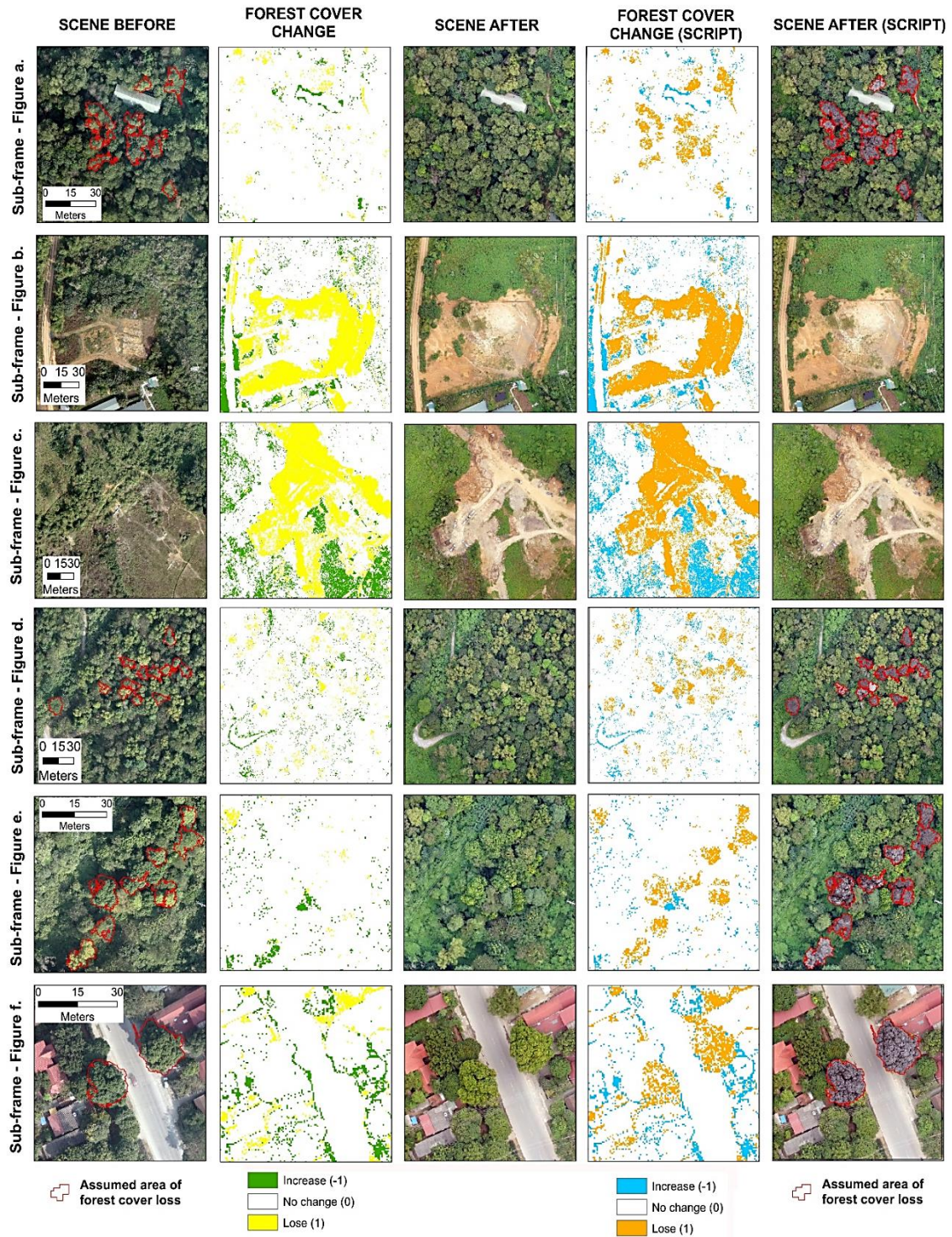
175

Figure 14. Visual comparison of the forest cover change map generated from the DNN model in the study area

Based on the forest cover change maps for the deforestation scenario (Fig. 13), a detailed analysis was conducted in six representative areas at the sub-frames (Figs. 13, 14). This analysis indicates that the forest cover change maps accurately reflect the images before and after classification (Fig. 14). In the sub-frames a, d, e, and f, the forest cover change maps clearly show areas that have experienced loss as outlined in the scenario (Fig. 14). The areas in sub-frames b and c indicate that the loss of forest cover is primarily due to human land development activities (Fig. 14). This highlights that human activity is a significant factor influencing the results of the land cover analysis, with water surface area increasing by 0.56%, while the 'Trees' class decreased by 0.33% (Table 4). Additionally, the errors generated by the model and the differences in evaluation results across various classes of the land cover classification map also contribute to the discrepancies observed in the forest cover change maps (Figs. 8-10; Table 3).

Despite UAVs' numerous benefits, there are still technical and legal challenges (Jiang, Yang and Song, 2020; Lambertini et al., 2022; Stöcker et al., 2017). The flight capabilities of UAVs are limited in terms of time and space, particularly in large and complex forested areas (Fraser and Congalton, 2018; Guimarães et al., 2020; Mohan et al., 2021). Additionally, airspace regulations in certain countries hinder the widespread deployment of UAVs (Cho, 2013; Xu et al., 2020). Future research directions should focus on enhancing flight capabilities, improving image quality, reducing costs, and developing automated data processing methods for UAV data, especially utilizing deep learning for large-scale data analysis (Osco et al., 2021; Shakhatreh et al., 2019; Telli et al., 2023). Moreover, we propose that integrating additional sensors for different spectral channels beyond RGB on UAVs, such as LiDAR and high-frequency spectral channels,

combined with terrain, geomorphological, and geological data, significantly improve the effectiveness and accuracy of deep learning models in analyzing and assessing forest cover changes.

Although many of the challenges above persist in the study of forest cover changes, this research provides a significant scientific foundation by proposing a process that integrates DNN modeling with GIS analysis and high-resolution UAV RGB imagery for evaluating and creating forest cover change maps. The results of the forest cover change maps demonstrate reliable accuracy, making them an essential tool for managers in management, planning, and conservation, as well as sustainable forest development in the Nui Luot study area.

6. Conclusions

This study successfully developed a process for generating forest cover change maps based on a DNN model, GIS analysis, and high-resolution UAV RGB data. This process is recommended for use in other areas for mapping and assessing forest cover changes.

The DNN model demonstrated strong classification capabilities with high accuracy in land cover classification in the Nui Luot area. The accuracy on the validation dataset for the before scene showed an average AUC of 0.922, ACC of 76.86%, average Precision of 0.743, average Recall of 0.73, average F1-Score of 0.723, Kappa of 0.692, and RMSE of 0.297. For the after scene, the accuracy was an average AUC of 0.954, ACC of 81.89%, average Precision of 0.823, average Recall of 0.815, average F1-Score of 0.818, Kappa of 0.758, and RMSE of 0.262.

The experimental study area at Nui Luot from January 31, 2023, to October 20, 2023, showed changes in land cover, with the 'Trees' class decreasing by 0.33%, the 'Vacant' class increasing by 1.44%, the 'Built area and

others' class decreasing by 1.68%, and the 'Water surface' class increasing by 0.56%. The primary causes of these land cover changes are human activities and variations in climatic conditions over time.

The land cover and forest cover change maps exhibit high accuracy. These tools are essential and beneficial for authorities in managing and conserving forests in the study area.

Further detailed research and development of new processing techniques and models are necessary to minimize calculation and classification errors in assessing and mapping land cover and forest cover changes.

Acknowledgments

References

Aldahdooh A., Hamidouche W., Fezza S.A., Déforges O., 2022. Adversarial example detection for DNN models: a review and experimental comparison. Artificial Intelligence Review, 55, 4403–4462.

Annus Z., Muhammad M.G., Muhammad S., Christian W., Muhammad I.M., Faisal S., Norbert W., 2021. AI-ForestWatch: semantic segmentation-based end-to-end framework for forest estimation and change detection using multi-spectral remote sensing imagery. Journal of Applied Remote Sensing, 15(2), 024518, 21p.

Bourgoin C., Betbeder J., Couteron P., Blanc L., Dessard H., Oszwald J., Le Roux R., Cornu G., Reymondin L., Mazzei L., Sist P., Läderach P., Gond V., 2020. UAV-based canopy textures assess changes in forest structure from long-term degradation. Ecological Indicators, 115, 106386.

Buchelt A., Adrowitzer A., Kieseberg P., Gollob C., Nothdurft A., Eresheim S., Tschiatschek S., Stampfer K., Holzinger A., 2024. Exploring artificial intelligence for applications of drones in forest ecology and management. Forest Ecology and Management, 551, 121530.

Camarretta N., Harrison P.A., Bailey T., Potts B., Lucieer A., Davidson N., Hunt M., 2020. Monitoring forest structure to guide adaptive management of forest restoration: a review of remote sensing approaches. New Forests, 51, 573–596.

Caputo T., Bellucci Sessa E., Marotta E., Caputo A., Belviso P., Avvisati G., Peluso R., Carandente A., 2023. Estimation of the Uncertainties Introduced in Thermal Map Mosaic: A Case of Study with PIX4D Mapper Software, Remote Sensing, 15(18), 4385. https://doi.org/10.3390/rs15184385.

Chenyan T., Zijun C., Ailin L., Zijun C., Xintian Z., 2024. Accuracy assessment of Mavic 3 industrial UAV based on DJI Terra and Pix4Dmapper, Proc. SPIE, 1322321. https://doi.org/10.1117/12.3035344.

Cho G., 2013. Unmanned aerial vehicles: Emerging policy and regulatory issues. Journal of Law, Information and Science, 22, 201–236.

Cochard R., Ngo D.T., Waeber P.O., Kull C.A., 2016. Extent and causes of forest cover changes in Vietnam's provinces 1993–2013: a review and analysis of official data. Environmental Reviews, 25, 199–217.

Dainelli R., Toscano P., Di Gennaro S.F., Matese A., 2021. Recent Advances in Unmanned Aerial Vehicle Forest Remote Sensing A Systematic Review. Part I: A General Framework, Forests, 12(4), 397. https://doi.org/10.3390/f12040397.

de la Torre J., Puig D., Valls A., 2018. Weighted kappa loss function for multi-class classification of ordinal data in deep learning. Pattern Recognition Letters, 105, 144–154.

Diez Y., Kentsch S., Fukuda M., Caceres M.L., Moritake K., Cabezas M., 2021. Deep Learning in Forestry Using UAV-Acquired RGB Data: A Practical Review, Remote Sensing, 13(14), 2837. https://doi.org/10.3390/rs13142837.

Draszawka K., Szymański J., 2023. From Scores to Predictions in Multi-Label Classification: Neural Thresholding Strategies, Applied Sciences, 13(13), 7591. https://doi.org/10.3390/app13137591.

Du M., Liu N., Song Q., Hu X., 2018. Towards Explanation of DNN-based Prediction with Guided Feature Inversion, Proceedings of the 24th ACM SIGKDD International Conference on Knowledge

Discovery & Data Mining. Association for Computing Machinery, London, United Kingdom, 1358–1367.

Ecke S., Dempewolf J., Frey J., Schwaller A., Endres E., Klemmt H.-J., Tiede D., Seifert T., 2022. UAV-Based Forest Health Monitoring: A Systematic Review, Remote Sensing, 14(13), 3205. https://doi.org/10.3390/rs14133205.

Faker O., Dogdu E., 2019. Intrusion Detection Using Big Data and Deep Learning Techniques, Proceedings of the 2019 ACM Southeast Conference. Association for Computing Machinery, Kennesaw, GA, USA, 86–93.

Fraser B.T., Congalton R.G., 2018. Issues in Unmanned Aerial Systems (UAS) Data Collection of Complex Forest Environments, Remote Sensing, 10(6), 908. https://doi.org/10.3390/rs10060908.

Giang Linh T., Dang Kinh B., Bui Thanh Q., 2023. Coastline and shoreline change assessment in sandy coasts based on machine learning models and high-resolution satellite images. Vietnam Journal of Earth Sciences, 45(2), 251–270. https://doi.org/10.15625/2615-9783/18407.

Grubesic T.H., Nelson J.R., Wei R., 2024. UAV Operating Environments, In: Grubesic, T.H., Nelson, J.R., Wei, R. (Eds.), UAVs for Spatial Modelling and Urban Informatics. Springer International Publishing, Cham, 17–32.

Guimarães N., Pádua L., Marques P., Silva N., Peres E., Sousa J.J., 2020. Forestry Remote Sensing from Unmanned Aerial Vehicles: A Review Focusing on the Data, Processing and Potentialities, Remote Sensing, 12(6), 1046. https://doi.org/10.3390/rs12061046.

Hansen M.C., Loveland T.R., 2012. A review of large area monitoring of land cover change using Landsat data. Remote Sensing of Environment, 122, 66–74.

Haq B., Jamshed M.A., Ali K., Kasi B., Arshad S., Kasi M.K., Ali I., Shabbir A., Abbasi Q.H., Ur-Rehman M., 2024. Tech-Driven Forest Conservation: Combating Deforestation With Internet of Things, Artificial Intelligence, and Remote Sensing. IEEE Internet of Things Journal, 11, 24551–24568.

Henry M., Réjou-Méchain M., Jara M.C., Wayson C., Piotto D., Westfall J., Fuentes J.M.M., Guier F.A., Lombis H.C., López E.C., Lara R.C., Rojas K.C., Del Águila Pasquel J., Montoya Á.D., Vega J.F., Galo A.J., López O.R., Marklund L.G., Milla F., de Jesús Návar Cahidez J., Malavassi E.O., Pérez J., Zea C.R., García L.R., Pons R.R., Sanquetta C., Scott C., Zapata-Cuartas M., Saint-André L., 2015. An overview of existing and promising technologies for national forest monitoring. Annals of Forest Science, 72, 779–788.

Hill S.L.L., Arnell A., Maney C., Butchart S.H.M., Hilton-Taylor C., Ciciarelli C., Davis C., Dinerstein E., Purvis A., Burgess N.D., 2019. Measuring Forest Biodiversity Status and Changes Globally. Frontiers in Forests and Global Change, 2, 11. https://doi.org/10.3389/ffgc.2019.00070.

Hussain H., Tamizharasan P.S., Rahul C.S., 2022. Design possibilities and challenges of DNN models: a review on the perspective of end devices. Artificial Intelligence Review, 55, 5109–5167.

Isaienkov K., Yushchuk M., Khramtsov V., Seliverstov O., 2021. Deep Learning for Regular Change Detection in Ukrainian Forest Ecosystem With Sentinel-2. IEEE Journal of Selected Topics in Applied Earth Observations and Remote Sensing, 14, 364–376.

Janga B., Asamani G.P., Sun Z., Cristea N., 2023. A Review of Practical AI for Remote Sensing in Earth Sciences, Remote Sensing, 15(16), 4112. https://doi.org/10.3390/rs15164112.

Jiang B., Yang J., Song H., 2020. Protecting Privacy From Aerial photography: State of the Art, Opportunities, and Challenges, IEEE INFOCOM 2020 - IEEE Conference on Computer Communications Workshops (INFOCOM WKSHPS), 799–804.

Khan S.H., He X., Porikli F., Bennamoun M., 2017. Forest Change Detection in Incomplete Satellite Images With Deep Neural Networks. IEEE Transactions on Geoscience and Remote Sensing, 55, 5407–5423.

Khelifi L., Mignotte M., 2020. Deep Learning for Change Detection in Remote Sensing Images: Comprehensive Review and Meta-Analysis. IEEE Access, 8, 126385–126400.

Kim D.-H., Sexton J.O., Noojipady P., Huang C., Anand A., Channan S., Feng M., Townshend J.R., 2014.

Global, Landsat-based forest-cover change from 1990 to 2000. Remote Sensing of Environment, 155, 178–193.

Lambertini A., Mandanici E., Tini M.A., Vittuari L., 2022. Technical Challenges for Multi-Temporal and Multi-Sensor Image Processing Surveyed by UAV for Mapping and Monitoring in Precision Agriculture, Remote Sensing, 14(19), 4954. https://doi.org/10.3390/rs14194954.

Lang S., Bravo-Marquez F., Beckham C., Hall M., Frank E., 2019. WekaDeeplearning4j: A deep learning package for Weka based on Deeplearning4j. Knowledge-Based Systems, 178, 48–50.

Lechner A.M., Foody G.M., Boyd D.S., 2020. Applications in Remote Sensing to Forest Ecology and Management. One Earth, 2, 405–412.

LeCun Y., Bengio Y., Hinton G., 2015. Deep learning. Nature, 521, 436–444.

Li L., Chen J., Mu X., Li W., Yan G., Xie D., Zhang W., 2020. Quantifying Understory and Overstory Vegetation Cover Using UAV-Based RGB Imagery in Forest Plantation, Remote Sensing, 12(2), 298. https://doi.org/10.3390/rs12020298.

Liu T., Sun Y., Wang C., Zhang Y., Qiu Z., Gong W., Lei S., Tong X., Duan X., 2021. Unmanned aerial vehicle and artificial intelligence revolutionizing efficient and precision sustainable forest management. Journal of Cleaner Production, 311, 127546.

Liu W., Wang Z., Liu X., Zeng N., Liu Y., Alsaadi F.E., 2017. A survey of deep neural network architectures and their applications. Neurocomputing, 234, 11–26.

Marín A.I., Abdul Malak D., Bastrup-Birk A., Chirici G., Barbati A., Kleeschulte S., 2021. Mapping forest condition in Europe: Methodological developments in support to forest biodiversity assessments. Ecological Indicators, 128, 107839.

Marom N.D., Rokach L., Shmilovici A., 2010. Using the confusion matrix for improving ensemble classifiers, 2010 IEEE 26th Convention of Electrical and Electronics Engineers in Israel, 000555–000559.

Maxwell A., Li R., Yang B., Weng H., Ou A., Hong H., Zhou Z., Gong P., Zhang C., 2017. Deep learning architectures for multi-label classification of intelligent health risk prediction. BMC Bioinformatics, 18, 523.

Mohan M., Richardson G., Gopan G., Aghai M.M., Bajaj S., Galgamuwa G.A.P., Vastaranta M., Arachchige P.S.P., Amorós L., Corte A.P., de-Miguel S., Leite R.V., Kganyago M., Broadbent E.N., Doaemo W., Shorab M.A., Cardil A., 2021. UAV-Supported Forest Regeneration: Current Trends, Challenges and Implications, Remote Sensing, 13(13), 2596. https://doi.org/10.3390/rs13132596.

Onishi M., Ise T., 2021. Explainable identification and mapping of trees using UAV RGB image and deep learning. Scientific Reports, 11, 903.

Ortega M.X., Bermudez J.D., Happ P.N., Gomes A., Feitosa R.Q., 2019. Evaluation of deep learning techniques for deforestation detection in the Amazon forest. Isprs Ann. Photogramm. Remote Sens. Spatial Inf. Sci., IV-2/W7, 121–128.

Osco L.P., Marcato Junior J., Marques Ramos A.P., de Castro Jorge L.A., Fatholahi S.N., de Andrade Silva J., Matsubara E.T., Pistori H., Gonçalves W.N., Li J., 2021. A review on deep learning in UAV remote sensing. International Journal of Applied Earth Observation and Geoinformation, 102, 102456.

Pham-Duc B., Tran Anh Q., Tong Si S., 2023. Monitoring monthly variation of Tonle Sap Lake water volume using Sentinel-1 imagery and satellite altimetry data. Vietnam Journal of Earth Sciences, 45(4), 479–496. https://doi.org/10.15625/2615-9783/18897.

Rithani M., Kumar R.P., Doss S., 2023. A review on big data based on deep neural network approaches. Artificial Intelligence Review, 56, 14765–14801.

Rodriguez-Galiano V.F., Chica-Rivas M., 2014. Evaluation of different machine learning methods for land cover mapping of a Mediterranean area using multi-seasonal Landsat images and Digital Terrain Models. International Journal of Digital Earth, 7, 492–509.

Samek W., Binder A., Montavon G., Lapuschkin S., Müller K.R., 2017. Evaluating the Visualization of What a Deep Neural Network Has Learned. IEEE Transactions on Neural Networks and Learning Systems, 28, 2660–2673.

Schiefer F., Kattenborn T., Frick A., Frey J., Schall P., Koch B., Schmidtlein S., 2020. Mapping forest tree species in high resolution UAV-based RGB-imagery

180

by means of convolutional neural networks. ISPRS Journal of Photogrammetry and Remote Sensing, 170, 205–215.

Shakhatreh H., Sawalmeh A.H., Al-Fuqaha A., Dou Z., Almaita E., Khalil I., Othman N.S., Khreishah A., Guizani M., 2019. Unmanned Aerial Vehicles (UAVs): A Survey on Civil Applications and Key Research Challenges. IEEE Access, 7, 48572–48634.

Shrestha A., Mahmood A., 2019. Review of Deep Learning Algorithms and Architectures. IEEE Access, 7, 53040–53065.

Stöcker C., Bennett R., Nex F., Gerke M., Zevenbergen J., 2017. Review of the Current State of UAV Regulations, Remote Sensing, 9(5), 459. https://doi.org/10.3390/rs9050459.

Telli K., Kraa O., Himeur Y., Ouamane A., Boumehraz M., Atalla S., Mansoor W., 2023. A Comprehensive Review of Recent Research Trends on Unmanned Aerial Vehicles (UAVs), Systems, 11(8), 400. https://doi.org/10.3390/systems11080400.

Tran Xuan T., Doan Thi Nam P., Le Thanh N., Viet-Ha N., Bui D.T., 2023. A novel HHO-RSCDT ensemble learning approach for forest fire danger mapping using GIS. Vietnam Journal of Earth Sciences, 45(3), 338–356. https://doi.org/10.15625/2615-9783/18500.

UN, 2024. Report on the technical assessment of the proposed forest reference level of Vanuatu submitted in 2023, Framework Convention on Climate Change 2024, 13p.

Watanabe M., Koyama C.N., Hayashi M., Nagatani I.,

Tadono T., Shimada M., 2021. Refined algorithm for forest early warning system with ALOS-2/PALSAR-2 ScanSAR data in tropical forest regions. Remote Sensing of Environment, 265, 112643.

Wei B., James K., 2013. Efficient Multi-label Classification with Many Labels. PMLR, 405–413.

Weisse M., Goldman E., Carter S., 2024. Forest Pulse: The Latest on the World's Forests, Global forest review. World resources institute, April, 2024. https://research.wri.org/gfr/latest-analysis-deforestation-trends.

Wu X.-Z., Zhou Z.-H., 2017. A Unified View of Multi-Label Performance Measures, In: Doina, P., Yee Whye, T. (Eds.), Proceedings of the 34th International Conference on Machine Learning. PMLR, Proceedings of Machine Learning Research, 3780–3788.

Xie Y., Wang Y., Sun Z., Liang R., Ding Z., Wang B., Huang S., Sun Y., 2024. Instance segmentation and stand-scale forest mapping based on UAV images derived RGB and CHM. Computers and Electronics in Agriculture, 220, 108878.

Xu C., Liao X., Tan J., Ye H., Lu H., 2020. Recent Research Progress of Unmanned Aerial Vehicle Regulation Policies and Technologies in Urban Low Altitude. IEEE Access, 8, 74175–74194.

Yang Q., Zhang H., Peng W., Lan Y., Luo S., Shao J., Chen D., Wang G., 2019. Assessing climate impact on forest cover in areas undergoing substantial land cover change using Landsat imagery. Science of The Total Environment, 659, 732–745.